PNAS RESEARCH ARTICLE | ASTRONOMY

Suppression of pair beam instabilities in a laboratory analogue of blazar pair cascades

Charles D. Arrowsmith[a,b,1], Francesco Miniati[a], Pablo J. Bilbao[c], Pascal Simon[d,e], Archie F. A. Bott[a], Stephane Burger[d], Hui Chen[f], Filipe D. Cruz[c], Tristan Davenne[g], Anthony Dyson[a], Ilias Efthymiopoulos[d], Dustin H. Froula[b], Alice Goillot[d], Jon T. Gudmundsson[h,i], Dan Haberberger[b], Jack W. D. Halliday[a,g], Tom Hodge[a,j], Brian T. Huffman[a], Sam Iaquinta[a], G. Marshall[j], Brian Reville[k], Subir Sarkar[a], Alexander A. Schekochihin[a], Luis O. Silva[c], Raspberry Simpson[f], Vasiliki Stergiou[a,d,l], Raoul M. G. M. Trines[g], Thibault Vieu[k], Nikolaos Charitonidis[d], Robert Bingham[g,m], and Gianluca Gregori[a]

Affiliations are included on p. 7.

Edited by Neta Bahcall, Princeton University, Princeton, NJ; received May 27, 2025; accepted October 6, 2025

The generation of dense electron–positron pair beams in the laboratory can enable direct tests of theoretical models of γ-ray bursts and active galactic nuclei. We have successfully achieved this using ultrarelativistic protons accelerated by the Super Proton Synchrotron at (CERN). In the first application of this experimental platform, the stability of the pair beam is studied as it propagates through a meter-length plasma, analogous to TeV γ-ray-induced pair cascades in the intergalactic medium. It has been argued that pair beam instabilities disrupt the cascade, thus accounting for the observed lack of reprocessed GeV emission from TeV blazars. If true, this would remove the need for a moderate strength intergalactic magnetic field to explain the observations. We find that the pair beam instability is suppressed if the beam is not perfectly collimated or monochromatic, hence the lower limit to the intergalactic magnetic field inferred from γ-ray observations of blazars is robust.

high-energy astrophysics | electron–positron pair cascades | blazar jets | plasma instabilities

Significance

In this work, a dense beam of electron–positron pairs is produced using protons accelerated by the Super Proton Synchrotron at CERN. The beam is propagated through an ambient plasma, analogous to pair cascades produced as blazar jets propagate through the intergalactic medium (IGM). It has been proposed that plasma instabilities disrupt these pair cascades, explaining the lack of secondary γ-rays observed from blazars. However, we find that under nonideal conditions likely to be relevant in the blazar context, pair beam instabilities are strongly suppressed and it is unlikely they play a significant role. This experimental study supports the hypothesis that the IGM contains a magnetic field of unknown origin that may well be a relic of the early Universe.

TeV-blazars are a class of active galactic nuclei (AGN) with relativistic jets pointing toward Earth that emit γ-rays with a hard spectrum extending to TeV energies (1). As the γ-rays propagate through the intergalactic medium (IGM), often through cosmic voids where matter exists as a tenuous, collisionless plasma, they are expected to scatter with extragalactic background light and trigger electromagnetic cascades of electron–positron ($e^{\pm}$) pairs. Subsequently, inverse-Compton scattering of the pairs with cosmic microwave background (CMB) photons is expected to produce a reprocessed spectrum of GeV energy γ-rays, but this is at odds with astronomical observations accumulated over more than a decade which have set stringent limits on the expected GeV γ-rays (2). The leading hypothesis is that $e^{\pm}$ pairs are deflected by intergalactic magnetic fields (IGMF) (3), spreading the GeV emission into diffuse halos that are not resolved by γ-ray telescopes (4, 5) [but may be detectable by the Cherenkov Telescope Array (6)]. However, the required strength and coherence length of the IGMF is sufficiently large that an astrophysical origin is unlikely; it may well be a relic of the early Universe (7–9). An alternative suggestion is that a substantial fraction of the pairs' energy is dissipated via electromagnetic beam–plasma instabilities (10–13) before the pairs inverse-Compton scatter with CMB photons (14, 15). Such instabilities lead to exponential amplification of electromagnetic fields via the unstable separation of electrons and positrons into current filaments. In extreme scenarios, they can lead to significant dissipation of the bulk kinetic energy and the onset of collisionless shocks. Whether these indeed play a role in the blazar-induced pair cascade and similar situations involving streaming $e^{\pm}$ pairs such as γ-ray bursts, depends on the initial linear stage of the instability (characterized by a linear growth rate) and the subsequent quasi-linear evolution which determines the transition to the saturation stage. When nonidealized conditions are considered, for example, finite divergence and energy spread, plasma kinetic theory suggests that beam–plasma instabilities may be strongly suppressed.

For relativistic pair beams with a low density compared with the ambient plasma, the fastest-growing modes of electromagnetic beam instability are oriented obliquely to the beam direction (16), with a characteristic scale comparable to the plasma skin depth, $\lambda_s = c/\omega_p$, where $\omega_p = (4\pi n_p e^2/m_e)^{1/2}$ is the plasma frequency, n_p is the ambient plasma electron density, e is the elementary charge, and m_e is the electron rest mass. The theoretical growth rate for a pair beam with a small angular spread $\Delta\theta = \Delta p_\perp/p_\parallel$ is given by (12):

The authors declare no competing interest.

This article is a PNAS Direct Submission.

[1]To whom correspondence may be addressed. Email: charles.arrowsmith@physics.ox.ac.uk.

This article contains supporting information online at https://www.pnas.org/lookup/suppl/doi:10.1073/pnas.2513365122/-/DCSupplemental.

Published November 7, 2025.

$$\Gamma = \frac{\sqrt{3}}{2^{4/3}}\,\omega_{\mathrm{p}}\left(\frac{n_\pm}{n_{\mathrm{p}}\gamma_\pm}\right)^{1/3}\left[\frac{k_\perp^{2/3}}{k^{2/3}} - \frac{3k_\perp^2}{8k_\parallel^2}(\Delta\theta)^2\left(\frac{2n_{\mathrm{p}}\gamma_\pm}{n_\pm}\right)^{2/3}\right], \quad [1]$$

where $k_\parallel$ and $k_\perp$ are the parallel and perpendicular components of the wave vector relative to the beam's propagation axis, $n_\pm$ is the pair number density and $\gamma_\pm$ is the relativistic Lorentz factor. The factor in square brackets accounts for transverse thermal motion of the beam, and tends to unity for a sufficiently collimated beam given $\Delta\theta \ll (n_\pm/n_{\mathrm{p}}\gamma_\pm)^{1/3}$, with the fastest-growing modes oriented transversely to beam propagation. However, if the transverse momentum spread is large enough, i.e. $\Delta\theta \gtrsim (n_\pm/n_{\mathrm{p}}\gamma_\pm)^{1/3}$, particle trajectories traverse the characteristic scale of unstable modes before current fluctuations can be amplified. The effect is to stabilize small-scale transverse modes, reduce the fastest growth rate, and tilt the direction of the fastest-growing mode toward the longitudinal direction. This is important in astrophysical contexts, where relativistic pair beams may be neither perfectly collimated nor monoenergetic. The purely transverse filamentation instability growth rate (scaling as $\Gamma \sim \omega_{\mathrm{p}}\sqrt{n_\pm/n_{\mathrm{p}}\gamma_\pm}$ (11)) only applies under very strict conditions, namely when the beam and return current are perfectly symmetric with the same density, temperature, and drift energies (17). If the angular spread is sufficiently large ($\Delta\theta > \Gamma\lambda_{\mathrm{s}}/c$) then the purely transverse filamentation modes are completely stabilized (18), whereas oblique unstable modes that lead to beam filamentation and magnetic field growth at an angle with respect to the beam distribution can still exist with a suppressed growth rate. In the kinetic regime, with very large transverse spreads the growth rate scales as $\Gamma \sim \omega_{\mathrm{p}}(n_\pm/n_{\mathrm{p}}\gamma_\pm)/(\Delta\theta)^2$ (19, 20), even more severely suppressed than predicted by Eq. **1**.

In order for pair beam instabilities to provide a plausible explanation for the observed lack of secondary GeV γ-rays from TeV blazars, the instability must lead to the generation of sufficiently large electromagnetic fields for a substantial fraction of the pairs' energy to be dissipated, or for pairs to be sufficiently deflected by self-generated fields that the secondary GeV emission is dispersed. This scenario has recently been discussed when considering whether the 400 GeV photon detected by Fermi from the "BOAT" GRB 221009A (21) may be generated from a TeV electromagnetic cascade in the IGM, a possibility consistent with the observation by LHAASO of γ-rays with energy up to 13 TeV from the direction of GRB 221009A (22). However, the short 33 ks time delay of the 400 GeV photon implies intergalactic magnetic fields significantly weaker than the lower bounds derived from blazar observations (5); this tension would be resolved if pair beam instabilities play a significant role. Nevertheless, it has been argued that suppression of the instability growth rates due to the large momentum spread of the cascade prevents their significant development before the pairs inverse-Compton scatter with CMB photons (23–25). This conjecture is difficult to verify using simulations due to their limited spatial and temporal range, nor has the theory been validated experimentally due to the challenge of producing pair beams with the necessary high density and quasi-neutrality (26). But experimental studies now become possible due to our recent breakthrough demonstration that relativistic $e^\pm$ pair beams can be efficiently produced using ultrarelativistic proton beams accelerated by the Super Proton Synchrotron (SPS) at CERN (27). Here, we investigate the stability of $e^\pm$ pair beams as they propagate through a meter-length ambient plasma to test whether the beam–plasma instabilities are indeed suppressed under nonidealized conditions, analogous to astrophysical situations involving $e^\pm$ pairs streaming through the IGM. We discuss the implications for blazar pair cascades in cosmic voids and comment on the robustness of the lower limit to the IGMF inferred from observations of blazar γ-ray spectra.

The experimental setup is shown in Fig. 1. More than 3×10^{11} protons are extracted from the SPS and delivered to the HiRadMat (High-Radiation to Materials) facility (28) with momentum 440 GeV/c in a single LHC-type bunch (transverse size $\sigma_r = 1$ mm and duration $\sigma_t = 0.25$ ns). The proton beam irradiates a custom-designed solid target consisting of a graphite rod with a tantalum converter. Hadronic interactions of the protons with carbon nuclei generates a copious number of neutral pions (π^0), which decay to produce a highly collimated beam of GeV-energy γ-rays. Inside the tantalum, the γ-rays trigger electromagnetic cascades of relativistic electron–positron pairs, leading to a secondary quasi-neutral beam containing over 10^{13} relativistic $e^\pm$ pairs, along with a much smaller number of protons and other secondary products (29). Characterization of the secondary beam is provided by Monte-Carlo simulations performed using FLUKA (30–32), a standard code capable of accurately describing hadronic and electromagnetic cascades in the target. The simulations are validated against luminescence screen measurements of the transverse beam profile and magnetic spectrometer measurements of the $e^\pm$ energy spectra (27). The pairs exhibit a multi-power-law spectrum in momentum, $dN_\pm/dE \propto E^{-m}$, with spectral index $m \approx 1-2$. The beam then propagates through an inductively coupled argon discharge plasma, with the plasma density and temperature measured prior to the experiment using a Langmuir probe, and confirmed noninvasively during the experiment using optical emission spectroscopy (details provided in *SI Appendix*). The plasma density is characterized by two identical bumps reaching a peak density of $n_{\mathrm{p}} = (1.8 \pm 0.1) \times 10^{12}\mathrm{cm}^{-3}$ when the discharge vessel is filled with argon to a pressure $p_{\mathrm{g}} = 4$ Pa and the inductive coils are supplied with 1 kW of radio-frequency power, corresponding to an absorbed power $P_{\mathrm{abs}} = 240 \pm 10$ W (33). Importantly, the physical size of the pair beam exceeds the expected size of current filaments (on the order of the plasma skin depth). Similar to many astrophysical situations, the ambient plasma is relativistically cold ($k_{\mathrm{B}}T_{\mathrm{e}} \sim$ eV), and the rates of electron-neutral collisions (ν_{en}) and electron–ion collisions (ν_{ei}) are much smaller than the plasma frequency (calculations in *SI Appendix*).

Since a collisionless kinetic description of the plasma applies to both the experiment and the astrophysical case, similarity scaling arguments may be applied (34). In this regard, we take care to consider the possible effects of the residual proton beam which accompanies the pair beam; though these protons are much smaller in number than the $e^\pm$ pairs, they remain localized to the central axis providing an additional current (and azimuthal magnetic field). We show in *SI Appendix* how the beam–plasma instability differs between our case and for pure, quasi-neutral $e^\pm$ jets. The residual current seeds the initial growth of the instability, but no other dynamical effects are observed and the instability grows at a comparable rate. Two main diagnostics are employed in the experiment: i) a time-resolved, magneto-optic Faraday rotation probe positioned near the end of the plasma to measure magnetic fields generated by pair beam instability, and ii) a chromium-doped alumina luminescence screen positioned downstream of the plasma to detect modulations in the transverse beam profile arising from the formation of electron/positron filaments (*Materials and Methods*).

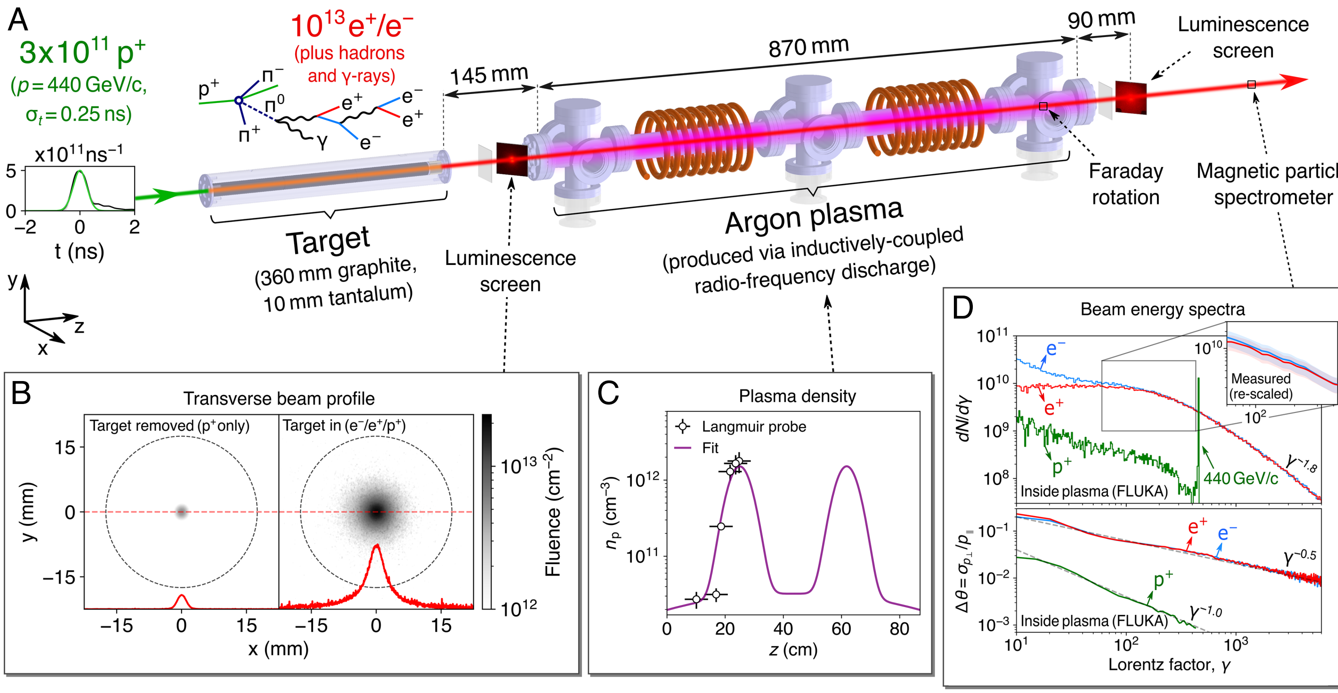

Fig. 1. Experimental setup. (*A*) Protons with 440 GeV/*c* momentum are extracted from the SPS accelerator with temporal profile measured using an integrating current transformer (*Inset*). The protons irradiate a solid target (360 mm graphite plus 10 mm tantalum) with a maximum fluence exceeding 3×10^{11} protons in a single bunch of duration 0.25 ns (1-σ) and transverse size $\sigma_r = 1$ mm. A secondary beam is generated via hadronic and electromagnetic cascades, containing a dominating fluence of electron–positron pairs ($N_{e^\pm} > 10^{13}$), plus hadrons, γ-rays and other secondaries. (*B*) Measurements of the transverse beam profile using 70 mm $\times$ 50 mm $\times$ 0.25 mm chromium-doped ceramic (Chromox) luminescence screens, viewed by a digital camera at a standoff distance of 3.8 m. The spatial resolution is limited to 100 μm by the Chromox translucence. (*C*) Downstream of the target, the beam passes though a meter-length argon plasma produced by an inductively coupled radio-frequency discharge. The longitudinal plasma density profile is measured using a Langmuir probe and confirmed during the experiment using optical emission spectroscopy. Pair beam filamentation due to beam–plasma instability is measured using a luminescence screen placed downstream of the plasma (camera positioned at a standoff distance 3.9 m), and a Faraday rotation diagnostic measures the growth of magnetic fields inside the plasma. (*D*) The electron and positron energy spectra are measured using a magnetic particle spectrometer (27), shown here rescaled according to the size of the collecting aperture to compare directly with FLUKA simulations of the spectra inside the plasma.

Experimental Results. The experimental results of both diagnostics are summarized in Fig. 2. The *Inset* of Fig. 2*A* shows the orientation of the magneto-optic terbium gallium garnet (TGG) crystal used to perform the Faraday rotation measurement, suspended in the plasma 81 cm downstream of the beam entry. A linearly polarized laser beam ($\lambda = 532$ nm) is passed twice through the TGG crystal, reflecting at the rear surface. Magnetic fields oriented along the length of the crystal will cause the polarization of the laser beam to rotate, which is detected by a time-resolved measurement of the intensity of the laser after passing through a second polarizing filter oriented at 45° to the initial polarization. The light is collected by a fast photodiode ($t_{10-90\%} = 0.44$ ns) and the measured intensity is given by $V = V_0 \cos^2(\langle B\rangle \mathcal{V} L + 45°)$, where $\langle B\rangle = \frac{2}{L}\int \mathbf{B}\cdot\hat{\mathbf{x}}\,dx$ is the mean component of the magnetic field along the propagation axis of the laser beam, $\mathcal{V} = 217 \pm 15$ rad T^{-1} m^{-1} is the measured Verdet constant, $L = 12$ mm is the length of the crystal, and $V_0 = 14$ mV is the intensity measured when the two polarizing filters are aligned and $\langle B\rangle = 0$. The prefactor of 2 accounts for the double pass of the crystal. Magnetic fields can be measured on the timescales of the beam duration ($t_{10-90\%} = 0.42$ ns) with a single-shot sensitivity limited to $B_{\rm sens} = 5$ mT by the intrinsic electronic noise (full characterization provided in *SI Appendix*). Since the timing is consistent between shots, the signal-to-noise ratio can be improved by combining signals from multiple shots. Five measurements of the pair beam are obtained and the mean intensity change (ΔV) and SD are plotted in Fig. 2*A*, showing that the maximum deviation of the mean signal corresponds to $\langle B\rangle = 5$ mT, weak enough that a precise measurement remains limited by the electronic noise floor. We infer an upper limit of the measured field of $\langle B\rangle_{\rm exp} \le 5$ mT, given that a value consistently larger than 5 mT in five repeated measurements leads to a statistically significant detectable signal (at the 2.2-σ level). An upper bound of the instability growth rate is estimated assuming that if the growth rate is sufficiently small then the magnetic field grows exponentially from the azimuthally oriented seed field, B_0, produced by the net current of the residual proton beam propagating on-axis: $\langle \Gamma_{\rm exp}\rangle = t_{\rm prop}^{-1} \log\left[\langle B\rangle_{\rm exp}/B_0\right] \le 0.7$ ns^{-1}, where $t_{\rm prop} = 2.7$ ns is the propagation time of the pair beam through plasma, and $B_0 = 0.78 \pm 0.13$ mT is calculated from the precise net current distribution obtained from a FLUKA simulation (as detailed in *SI Appendix*). For comparison, the beam instability growth rate calculated from linear kinetic theory (using Eq. **1**) assuming a perfectly collimated beam gives a linear growth rate $\Gamma = 2.0$ ns^{-1}, significantly higher than observed in the experiment.

It is possible that the Faraday probe measurement may underestimate the strength of the magnetic field if large-amplitude variations are present on scales smaller than the length of the Verdet crystal, however this would be accompanied by observations of strong separation of current in the measurements of the downstream transverse beam profile (Fig. 2*B*), for example, clear structures of the kind observed in particle-in-cell simulations of collimated pair beams presented in the next section. Instead, no difference is observed between the beam profiles with and without the plasma present. Low-contrast current separation

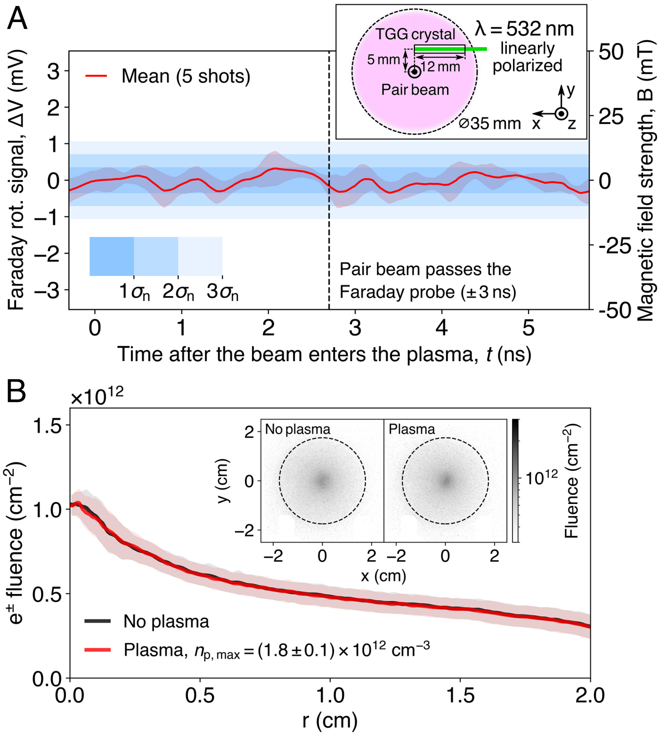

Fig. 2. Magnetic field and beam profile measurements. (*A*) Magnetic fields are measured at the end of the plasma using a time-resolved Faraday rotation technique. A linearly polarized laser beam ($\lambda = 532$ nm) is passed twice through a magneto-optic crystal (TGG, 12 mm length, 2 mm diameter), suspended in the plasma by a ceramic reentrant tube (orientation shown in the *Inset*), before passing through a second polarizing filter offset by 45° from the initial polarization. The change in laser intensity measured by a fast photodiode ($\Delta V = V - V_0/2$) is plotted as a function of time, with the pair beam expected to pass the probe 2.7 ns after the beam enters the plasma (the signal is shown a few ns before and afterward to account for the uncertainty in the exact timing). The mean signal from five shots is plotted, with corresponding SD represented by the red shaded region. The blue shaded regions show the SD of the intrinsic electronic noise. (*B*) The transverse beam profile is measured using a Chromox luminescence screen positioned 90 mm downstream of the plasma discharge. The residual primary proton beam is subtracted from the images (*Materials and Methods*), leaving the fluence of electron–positron pairs (plus additional secondaries). The radial lineouts are shown when the plasma is present ($p_g = 4$ Pa, $P_{abs} = 240 \pm 10$ W) and when there is no plasma ($p_g = 0.5$ Pa, $P_{abs} = 0$ W), with the image data shown in the *Inset*. The shaded regions represent the SD of the lineout pixel counts combined with the uncertainty in the absolute calibration.

can be obscured due to the equal sensitivity of the screen to electrons and positrons, but the development of high-contrast, millimeter-scale filaments can be ruled out, and a slower-than-expected growth rate remains the most plausible explanation. We attribute the reduced growth rate to suppression due to the finite thermal spread of the pairs, and we show in the following section that particle-in-cell simulations predict that the instability of collimated, monoenergetic pairs would instead produce much stronger, measurable magnetic fields. A reduction of the pair beam's density as it diverges may also cause the growth rate to be reduced, but theoretical calculations indicate that this cannot explain the full extent of the observed suppression. Additional measurements were performed with lower peak plasma densities and with the probe oriented to point in a radial direction to the beam path (presented in *SI Appendix*). In all cases, similarly weak magnetic fields were observed.

Particle-in-Cell Simulations. The effects of finite thermal spread of the $e^\pm$ pairs are explored further by performing three-dimensional (3D3V) particle-in-cell (PIC) simulations using the fully relativistic, massively parallel PIC code OSIRIS (35). In the simulations, a moving window follows an electron–positron–proton beam at the speed of light to model conditions closely resembling the experimental pair beam and the ambient plasma (*Materials and Methods*). Given the initial charge and current distribution of the beam species (electron, positrons, and protons), as determined from the FLUKA simulations, the corresponding self-consistent fields are determined by solving Poisson's equations in the beams' proper frame, and then Lorentz boosting these fields back to the laboratory frame, ensuring the fields are self-consistently coupled to the beams. The idealized case of a perfectly collimated monoenergetic pair beam is considered for comparison. In simulations performed without the residual primary protons, a quasi-neutral pair beam is observed to filament with fluctuations that grow from thermal noise without regard for the central axis (as shown in additional simulations presented in *SI Appendix*). When they are included, the protons copropagate on-axis providing a seed magnetic field for the instability, which causes the positron density to increase on-axis and the azimuthal magnetic field to be amplified exponentially with the same growth rate. Otherwise, the protons do not play a dynamical role during the experiment timescale because of their much larger inertia. When identical simulations are performed without a background plasma, instabilities are no longer observed.

The results are shown in Fig. 3. In both cases, current separation of electrons and positrons is observed on the scale of the plasma skin depth. In the case where the $e^\pm$ pairs are collimated and monoenergetic, the filaments become completely separated and emerge on much smaller spatial scales. The peak magnetic field is vastly increased ($B_{max} = 60$ mT) with a peak growth rate $\Gamma_{sim} = 2.1$ ns^{-1}, well-matched by the theoretical prediction for a cold pair beam ($\Gamma = 2.0$ ns^{-1}, Eq. **1**). By contrast, when the finite thermal spread of pairs is accounted for, the small-scale modes are stabilized, and the peak magnetic field and growth rate are significantly reduced ($B_{max} = 7$ mT, $\Gamma_{sim} = 0.2$ ns^{-1}). The simulated magnetic fields provide a prediction of the Faraday rotation measurement of $\langle B \rangle_{sim} = 1.7$ mT, leading to an estimated average growth rate $\langle \Gamma_{sim} \rangle = 0.3$ ns^{-1}, consistent with the experimentally obtained bound $\langle \Gamma_{exp} \rangle \leq 0.7$ ns^{-1}.

Discussion. To assess whether beam–plasma instabilities are important for blazar-induced pair beams propagating through cosmic voids, a maximum growth rate of the instability is estimated by scaling the experimental upper bound on the growth rate according to Eq. **1**. The pair density and energy spectrum of a typical blazar pair cascade are estimated using a Monte-Carlo model, described in Elyiv et al. (36) and used by e.g. Neronov and Vovk (3) and Miniati and Elyiv (23) (modeled parameters given in Table 1). The blazar spectral emission is assumed to be a power-law distribution, $dN_\gamma/dE_\gamma \propto E_\gamma^{-1.8}$ in the range $10^3 \leq E_\gamma/m_e c^2 \leq 10^8$, with equivalent isotropic luminosity 10^{45} erg s^{-1}, using a model for the extragalactic background light described by Aharonian (37). The pair density obtained is model dependent, but $n_{\pm,blz} \sim 10^{-23}\,(1+z)^{9.5}$ cm^{-3} (14, 23) is considered to be reasonable, where z is the redshift. This redshift dependence is expected to be valid for TeV blazars with $z \lesssim 1$ (14). The mean Lorentz factor of pairs is $\langle \gamma_\pm \rangle \sim 10^5$, while pairs that inverse-Compton scatter with CMB photons to produce GeV emission have a much higher Lorentz factor ($\gamma_\pm \sim 10^7$). The density of free electrons in the void is estimated

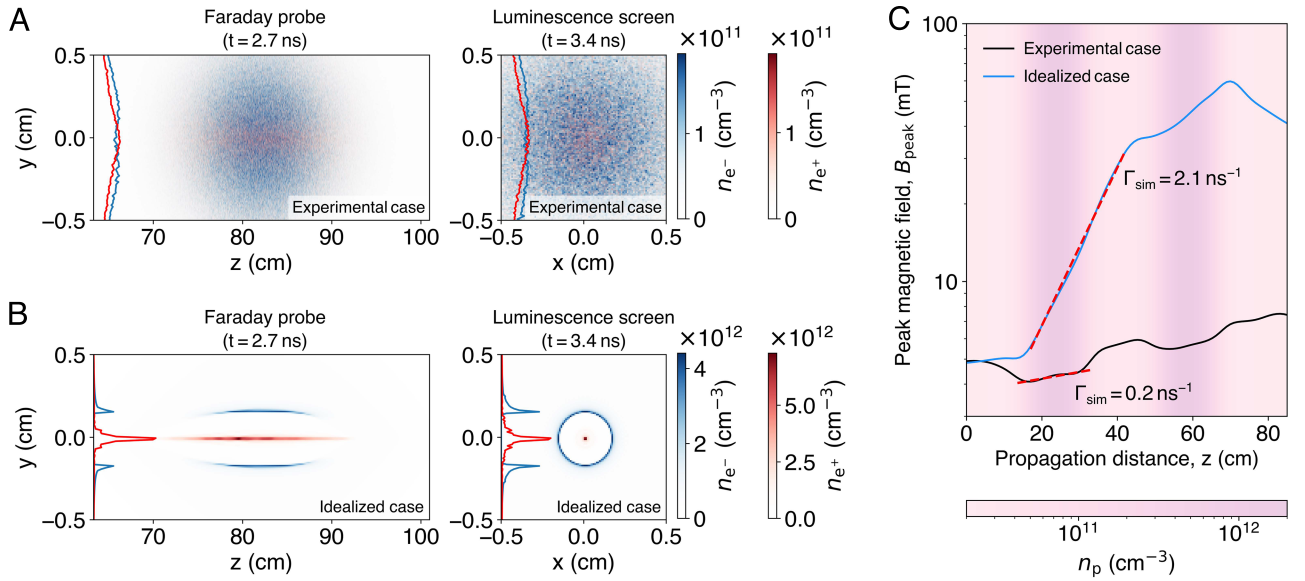

Fig. 3. Three-dimensional particle-in-cell simulations. 3D simulations of the beam–plasma interaction are performed using the particle-in-cell code OSIRIS (35) for two cases: (*A*) with conditions closely resembling the experimental beam and ambient plasma (labeled "experimental"), and (*B*) an idealized case with a collimated, monoenergetic ($\gamma_\pm = 10^3$) pairs (labeled "idealized"). In (*A* and *B*), the *Left* panels show a central slice of the electron and positron densities in the longitudinal plane (*y*-*z*) at the time when the beam passes the Faraday probe (t = 2.7 ns after entering the plasma), while the *Right* panels show a central slice of the transverse plane (*x*-*y*) when the beam passes the downstream luminescence screen (t = 3.4 ns). (*C*) The peak magnetic field is plotted as a function of propagation distance through the plasma, with the background shading showing the ambient plasma density. The maximum growth rate of the peak magnetic field is obtained by the shown fits (red-dashed). The anticorrelation of magnetic field and plasma density is an effect of the varying level of return current.

by $n_{\mathrm{p,IGM}} = \Omega_b f_{\mathrm{IGM}} \rho_c / m_p$, where Ω_b is the cosmological baryon density parameter, f_{IGM} is the relative fraction of baryons in the IGM, m_p is the proton rest mass, and $\rho_c = 3H_0^2/8\pi G$ is the critical mass density of the Universe, where H_0 is the Hubble constant and G is the gravitational constant. The IGM is assumed to be fully ionized (38). The fraction of baryons in the IGM, f_{IGM}, is constrained by measurements of the dispersion measure of extragalactic fast radio bursts to be $f_{\mathrm{IGM}} \approx 0.4 - 0.8$ (39, 40) [more recently, $f_{\mathrm{IGM}} = 0.76^{+0.10}_{-0.11}$ (41)]. A void density $n_{\mathrm{p,IGM}} = 2 \times 10^{-7}\,(1+z)^3\,\mathrm{cm}^{-3}$ is obtained by assuming $f_{\mathrm{IGM}} = 0.8$ and using standard cosmological parameters from Planck (42): $\Omega_b h^2 = 0.02237 \pm 0.00015$, where $h = H_0/100\,\mathrm{km\,s^{-1}\,Mpc^{-1}}$.

Under these conditions, electromagnetic beam instability is strongly suppressed ($\Delta\theta \gg (n_\pm/n_p\gamma_\pm)^{1/3}$), and we can scale the linear growth rate according to Eq. **1** in the limit of large $\Delta\theta$ ($\Gamma = \sqrt{2/3}\,\omega_p (n_\pm/2n_p\gamma_\pm)^{2/3}/(\Delta\theta)$):

$$\Gamma_{\mathrm{blz}}\,[\mathrm{s}^{-1}] \le 4 \times 10^{-10} \left(\frac{\Gamma_{\exp}}{0.7\ \mathrm{ns}^{-1}}\right). \qquad \textbf{[2]}$$

This estimate likely overestimates the growth rate of the oblique filamentation instability, comparing it to predictions for the kinetic regime where the equivalent scaling gives $\Gamma_{\mathrm{blz}} \le 2 \times 10^{-13}\mathrm{s}^{-1}$. Assuming the more conservative bound, the linear growth timescale ($\tau_{\mathrm{ins}} \equiv 1/\Gamma_{\mathrm{blz}}$) is plotted in Fig. 4 alongside estimates of the fastest growth rate for a collimated, monoenergetic blazar-jet pair cascade and the inverse-Compton cooling time of pairs with CMB photons:

$$\tau_{\mathrm{IC}}\,[\mathrm{s}] = 3.8 \times 10^{13} \left(\frac{E_e}{1\ \mathrm{TeV}}\right)^{-1} (1+z)^{-4}. \qquad \textbf{[3]}$$

For blazar-jet pair densities in the range $n_{\pm,\mathrm{blz}} = 10^{-25} - 10^{-21}\mathrm{cm}^{-3}$, we find that the scaled suppressed growth rate may still be fast compared with the inverse-Compton cooling rate. However, the saturated strength of magnetic fields is limited by the particle-trapping condition (43). That is, magnetic field generation is expected to saturate when the frequency at which particles "bounce" between magnetic filaments is comparable to the instability growth rate prior to saturation, i.e., when $\omega_B \sim \Gamma$, where $\omega_B \sim v/\sqrt{\lambda_B r_g}$, v is the particle velocity, λ_B is the length scale of magnetic filaments and r_g is the gyroradius. Assuming λ_B is comparable to the skin depth of the ambient plasma (17, 44):

$$B_{\perp,\mathrm{sat}}\,[\mathrm{mT}] \lesssim 4 \times 10^{-24} \left(\frac{\Gamma_{\mathrm{blz}}}{4 \times 10^{-10}\mathrm{s}^{-1}}\right)^2. \qquad \textbf{[4]}$$

We compare this field strength in Fig. 4 with lower limits on the IGMF imposed by the lack of observed GeV cascade emission

Table 1. Pair cascade and plasma parameters in the experiment and for a typical blazar jet in the cosmic void (luminosity 10^{45} erg s^{-1}, at a distance 300 Mpc)

Parameter	Experiment	Typical blazar jet
Plasma		
Ambient plasma density, n_p (cm^{-3})	10^{12}	2×10^{-7}
Skin depth, c/ω_p (m)	5×10^{-3}	10^7
Collisionality, ν_e/ω_p	10^{-3}	10^{-13}
Pair cascade		
Pair density, $n_\pm$ (cm^{-3})	5×10^{10}	10^{-23}
Mean Lorentz factor, $\langle\gamma_\pm\rangle$	10^3	10^5
Transverse momentum spread, $\Delta\theta$	0.025	10^{-4}

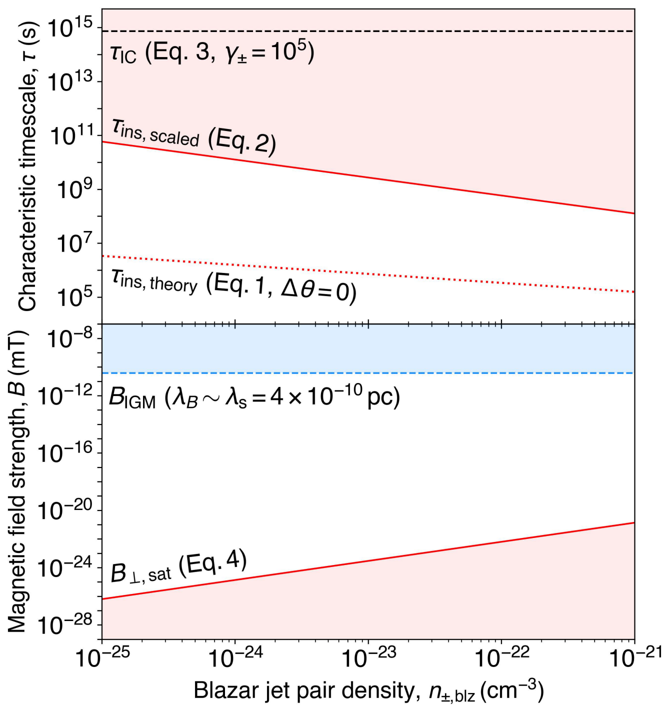

Fig. 4. Characteristic timescales and magnetic field strengths relevant to blazar-induced pair cascades in cosmic voids. *Upper* panel: The experimentally obtained bound on the growth rate of electromagnetic pair beam instability ($\Gamma_{\text{exp}} \leq 0.7\,\text{ns}^{-1}$) is scaled using Eq. **2** to obtain a lower bound on the linear growth rate for blazar-induced pair beams propagating through cosmic void (red solid). The growth timescale is much larger than theoretical predictions assuming a collimated, monoenergetic pair beam (Eq. **1**, $\Delta\theta = 0$, red dotted), but short compared with the inverse-Compton cooling time of pairs with CMB photons (Eq. **3**, $\gamma_\pm = 10^5$, black-dashed). *Lower* panel: The maximum strength of the magnetic field at instability saturation is inferred assuming the experimentally obtained bound on the growth rate (Eq. **4**, red solid). The field strengths are incompatible with lower bounds inferred from blazar spectral measurements for a coherence length comparable to the ambient skin depth (blue-dashed). It is assumed in all cases that the redshift is $z \lesssim 1$.

in Fermi/LAT and MAGIC telescope data: $B_{\text{IGM}}\,[\text{mT}] \geq 4 \times 10^{-11}\,(\lambda_B/4 \times 10^{-10}\text{pc})^{-1/2}$. We find that even if many *e*-folding lengths of instability can develop, the generated magnetic fields are much too small to explain the required angular spreading. After saturation of electromagnetic modes, longitudinal electrostatic oscillations may continue to grow at the slower quasi-linear rate (19), but the velocity spread of pairs is much too large to allow significant coupling of the pair beam's kinetic energy into large-amplitude, resonantly driven plasma waves (i.e. $k \cdot \Delta v_\pm \gg \Gamma$). We can therefore rule out that beam–plasma instabilities plausibly affect TeV blazar pair cascades; hence, the inferred lower bound on the intergalactic magnetic field strength is robust.

Materials and Methods

Electron–Positron Pair Production Target. The target used to produce the secondary beam consists of a 360 mm length cylinder of isostatic graphite (SGL Carbon R6650, 1.84 g cm^{-3}) and a 10 mm thickness tantalum converter, both with a diameter of 20 mm. The graphite and tantalum are encased inside a 400 mm length, 50 mm diameter cylinder of high-strength T9 aluminum alloy that acts as both a confinement vessel and a heat sink. The tantalum is press-fit to ensure maximal thermal contact. 2 mm thickness expanded graphite pieces (SGL Carbon Sigraflex, 1 g cm^{-3}) separate the target components to allow thermal expansion and reduce contact stresses during irradiation, while 2 mm thickness Sigradur G glassy carbon beam windows are clamped onto either end of the target by aluminum flanges with Viton O-rings to seal the target materials hermetically. Radiative and convective cooling via the outer surface of the target housing leads to cooling of the target to room temperature within a few seconds following the beam impact, while the beam-induced maximum strain of the tantalum remains in all cases well below its plastic deformation limit, i.e. the target is not destroyed when irradiated by the proton beam and can be reused for many (potentially thousands of) shots.

Inductively Coupled Argon Plasma Discharge. The plasma discharge is composed of a vacuum chamber constructed from three six-way port crosses (nonferrous, 304L-grade stainless steel), separated by two sections of glass tube (15 cm length), terminated at each end by a 4 mm-thick glassy carbon beam window. The total length of the discharge region is $L = 87$ cm, with an inner diameter $d = 3.5$ cm. Inductive coils wrap around the sections of glass tube (1 cm diameter copper pipe, with 8.5 turns, and coil-winding inner diameter 7.5 cm). The coils and surrounding metallic segments of the chamber are connected to a zero ground potential. The vacuum pump, argon gas line, and Faraday probe are attached at the port crosses. Before operation, the chamber is evacuated to a base pressure $p_{\text{g,base}} = 5$ mPa, before filling with argon gas (purity 99.999%) to a pressure $p_{\text{g}} = 4$ Pa. Radio-frequency power is supplied to the coils at a frequency $f = 13.56$ MHz using a commercially available 1 kW radio-frequency power generator (Advanced Energy CESAR 1310) via an impedance-matching network (Advanced Energy Navio). The power absorbed by the plasma corresponds to approximately 25% of the supplied power. A plasma is produced by inductive coupling inside the coils with plasma density exceeding $n_{\text{p}} \gtrsim 1 \times 10^{12}\text{cm}^{-3}$, while a lower-density plasma ($n_{\text{p}} \sim 10^{10} - 10^{11}\text{cm}^{-3}$) is sustained between the coils by electrostatic/capacitive coupling. The discharge is ignited several seconds before the beam's arrival and is deactivated several seconds after the beam has passed. Further details and extensive plasma characterization are provided in ref. 33.

Time-Resolved Magneto-Optic Faraday Rotation Probe. A continuous-wave diode laser (Z-Laser ZM18, $\lambda = 532$ nm, $P = 40$ mW) is transported to the Faraday probe's location via optical fiber and linearly polarized using a nanoparticle linear film polarizer, chosen for its high extinction ratio (10,000:1), high transmission ratio (73%) at $\lambda = 532$ nm and high damage threshold. The laser beam is split using a 50:50 beamsplitter and the transmitted beam is used as a reference beam to monitor changes in the intensity of the probe laser beam, while the reflected beam is directed transversely to the particle–beam axis through a 12 mm length, 2 mm diameter TGG magneto-optic crystal suspended in the plasma at the end of a ceramic reentrant tube (inner length 70 mm, outer diameter 5 mm). The crystal is positioned 81 cm into the plasma at a closest distance of 5 mm to the particle–beam axis (orientation shown in Fig. 2). The crystal has an antireflective coating on the front surface and a highly reflective coating on the rear surface to reflect the probe beam so that it makes a double pass of the crystal, thereby doubling the Faraday rotation for a given magnetic field. The reflected probe beam passes through a second linear polarizer oriented at a 45° angle to the first and is coupled into a 7 m length optical fiber (silica core, glass clad, step index with 0.22 NA, ø200 μm core). The light is collected by a 2 GHz bandwidth photodiode (Thorlabs DET025AFC/M) and a shielded coaxial cable connects the photodiode to a 3 GHz oscilloscope (LeCroy WavePro 7300A). A schematic of the design is provided in *SI Appendix* along with measurements of the Verdet constant, intrinsic noise, and instrument response function, measuring instrument sensitivity to magnetic fields of magnitude $B_{\text{sens}} = 5$ mT and a time resolution of 0.44 ns (10 to 90% rise time). The Verdet constant of the crystal is measured again at the end of the beam time to confirm that the instrument's sensitivity has not degraded due to radiation damage.

Chromium-Doped Alumina Luminescence Screens. Chromium-doped alumina-ceramic luminescence screens (Chromox, Al_2O_3: 99.5%, Cr_2O_3: 0.5%) are used to measure the transverse beam profile before and after the beam passes through the plasma. When energy is deposited in the screen by ionizing particles and radiation, luminescence light is emitted isotropically, strongest at wavelengths $\lambda_1 = 691$ nm, and $\lambda_2 = 694$ nm with decay times 3–6 ms. Screens are oriented at 45° to the beam path and viewed directly by a digital camera (Basler acA1920-40gm GigE camera with Sony IMX249 CMOS sensor and Canon EF 75 to 300 mm f/4-5.6 III lens) at a standoff distance 4 m with an exposure time 24 ms. It is reasonably assumed that the vast majority of particles incident on the screens are relativistic and deposit approximately the same amount of energy in a minimum-ionizing fashion. The spatial resolution is limited due to screen translucence to 100 μm (attenuation length, $\mu = 0.8$ mm^{-1}), capable of resolving the filament formation in the pair beam since the size of unstable modes is expected to be several mm. The screen downstream of the plasma is positioned $d_{\mathrm{scr}} = 90$ mm from the glassy carbon beam window, and a blocker foil (50 μm aluminum) is placed before the screen to minimize stray optical light. In Fig. 2, the residual protons in the transverse beam profile are subtracted from the raw image by fitting the proton peak to a 2D Gaussian with initial parameters $\sigma_x = \sigma_y = 1$ mm and integrated intensity corresponding to the expected number of residual primary protons that do not significantly scatter inelastically with the target, a fraction given by $N_{\mathrm{res}}/N_{\mathrm{inc}} = \exp(-L_{\mathrm{C}}/\lambda_{\mathrm{C}})\exp(-L_{\mathrm{Ta}}/\lambda_{\mathrm{Ta}}) = 0.42$, where $L_{\mathrm{C}} = 360$ mm and $L_{\mathrm{Ta}} = 10$ mm are the lengths of graphite and tantalum, and $\lambda_{\mathrm{C}} = 466$ mm and $\lambda_{\mathrm{Ta}} = 115$ mm are their corresponding nuclear interaction lengths. The calculation of N_{res} is in agreement with FLUKA Monte-Carlo simulations. Coulomb scattering of $\mathrm{e}^{\pm}$ pairs in the glassy carbon beam window is only expected to significantly affect the pairs with a much lower energy than the mean, with a point source diverging to a size $\sigma_{\mathrm{spread}} \approx 0.3$ mm $(\gamma_{\pm}/\langle\gamma_{\pm}\rangle)^{-1}$ (45).

Particle-in-Cell (PIC) Simulations. Three-dimensional (3D3V) PIC simulations were performed using the OSIRIS code at the exascale LUMI supercomputer (Finland). Simulations use a moving window traveling at c along the z-direction that follows relativistic electrons, positrons, and protons in the secondary beam as they propagate through the ambient plasma. The electron–positron–proton beam is initialized before entrance of the plasma, centered at $z = -20$ cm and $x = y = 0$. The density and momentum phase-space distributions are accurately modeled by fitting analytical forms to the distributions at the entrance of the plasma cell, after the glassy carbon window, obtained from a FLUKA simulation (as described in *SI Appendix*). The longitudinal density profile of the plasma is chosen to match closely the measured electron density profile of the plasma discharge (plotted alongside Langmuir probe data in the *Inset* of Fig. 1): double peaked with maximum plasma density $n_0 = 1.78 \times 10^{12}\mathrm{cm}^{-3}$ (functional form provided in *SI Appendix*). All quantities in the simulations are normalized to the peak plasma density n_0 (associated plasma period $\omega_{\mathrm{pe}}^{-1} = 13.29$ ps, and plasma skin-depth $c/\omega_{\mathrm{pe}} = 3.98$ mm). The moving window has absorbing boundary conditions and dimensions $L_x \times L_y \times L_z = 3.5$ cm $\times$ 3.5 cm $\times$ 40 cm, discretized into $879 \times 879 \times 10{,}050$ cells. This yields a spatial resolution $\Delta x = 0.01\, c/\omega_{\mathrm{pe}} = 0.096$ mm. The simulations employ a time resolution $\Delta t = 0.0057\, \omega_{\mathrm{pe}}^{-1} = 43.7$ fs, fulfilling the 3D Courant–Friedrichs–Lewy condition: $c\Delta t < \Delta x/\sqrt{3}$. We employ 8 macroparticles per cell (for each species), and utilize quadratic interpolation with first-order binomial current smoothing. The numerical parameters were carefully chosen after a convergence study with 2D3V PIC simulations.

Data, Materials, and Software Availability. All study data are included in the article and/or *SI Appendix*.

ACKNOWLEDGMENTS. We thank Prof. C. Joshi (University of California Los Angeles), Dr. F. Albert Lawrence Livermore National Laboratory (LLNL) and Dr. C. Densham (Science and Technology Facilities Council Rutherford Appleton Laboratory) for useful discussions, as well as T. Levens (European Organization for Nuclear Research) and Dr. T. Ma (LLNL) for supporting this experiment. This project has received funding from the European Union's Horizon Europe Research and Innovation programme under Grant Agreement No. 101057511 (EURO-LABS). The work of G.G. was partially supported by UK Research and Innovation (UKRI) under grants no. ST/W000903/1 and EP/Y035038/1, while A.F.A.B. was also supported by UKRI (grant no. MR/W006723/1). The work of P.J.B. and L.O.S. was supported by Foundation for Science and Technology (FCT) (Portugal)-Foundation for Science and Technology under the Project X-maser (No. 2022.02230.PTDC) and Grant No. UI/BD/151559/2021, as well as MareNostrum5 (Spain) funded by FCT project DOI: 10.54499/2024.07895.CPCA.A3. The work of D.H.F. and D.H. was supported by the U.S. Department of Energy under Award No. DE-NA0004144. The work of A.A.S. was supported in part by the Simons Foundation via a Simons Investigator Award. We also acknowledge funding from AWE plc., and the Central Laser Facility (STFC). FLUKA simulations were performed using the STFC Scientific Computing Department's SCARF cluster. OSIRIS simulations were performed at LUMI-C (Finland) within European High Performance Computing Joint Undertaking Project No. EHPC-REG-2021R0038.

Author affiliations: [a]Department of Physics, University of Oxford, Oxford OX1 3PU, United Kingdom; [b]University of Rochester Laboratory for Laser Energetics, Rochester, NY 14623; [c]GoLP/Instituto de Plasmas e Fusão Nuclear, Instituto Superior Técnico, Universidade de Lisboa, Lisboa 1049-001, Portugal; [d]European Organization for Nuclear Research (CERN), Geneva 23 CH-1211, Switzerland; [e]GSI Helmholtz Center for Heavy Ion Research, Helmholtzzentrum für Schwerionenforschung GmbH, Darmstadt 64291, Germany; [f]Lawrence Livermore National Laboratory, Livermore, CA 94550; [g]Science and Technology Facilities Council Rutherford Appleton Laboratory, Chilton, Didcot OX11 0QX, United Kingdom; [h]Science Institute, University of Iceland, Reykjavik IS-107, Iceland; [i]Division of Space and Plasma Physics, School of Electrical Engineering and Computer Science, KTH Royal Institute of Technology, Stockholm SE-100 44, Sweden; [j]AWE Nuclear Security Technologies, Aldermaston, Reading, Berkshire RG7 4PR, United Kingdom; [k]Max-Planck-Institut für Kernphysik, Heidelberg D-69117, Germany; [l]School of Applied Mathematics and Physical Sciences, National Technical University of Athens, Athens 157 72, Greece; and [m]Department of Physics, University of Strathclyde, Glasgow G4 0NG, United Kingdom

Author contributions: C.D.A., F.M., N.C., R.B., and G.G. designed research; C.D.A., F.M., P.J.B., P.S., A.F.A.B., S.B., H.C., F.D.C., T.D., A.D., I.E., D.H.F., A.G., J.T.G., D.H., J.W.D.H., T.H., B.T.H., S.I., G.M., B.R., S.S., A.A.S., L.O.S., R.S., V.S., R.M.G.M.T., T.V., N.C., R.B., and G.G. performed research; C.D.A. and P.J.B. analyzed data; and C.D.A., F.M., P.J.B., B.R., S.S., L.O.S., R.B., and G.G. wrote the paper.

1. G. D. Şentürk, M. Errando, M. Böttcher, R. Mukherjee, Gamma-ray observational properties of TeV-detected blazars. *Astrophys. J.* **764**, 119 (2013).
2. F. Aharonian *et al.*, A low level of extragalactic background light as revealed by γ-rays from blazars. *Nature* **440**, 1018–1021 (2006).
3. A. Neronov, I. Vovk, Evidence for strong extragalactic magnetic fields from Fermi observations of TeV blazars. *Science* **328**, 73–75 (2010).
4. S. Archambault *et al.*, Search for magnetically broadened cascade emission from blazars with VERITAS. *Astrophys. J.* **835**, 288 (2017).
5. M. Ackermann *et al.*, The search for spatial extension in high-latitude sources detected by the Fermi Large Area Telescope. *Astrophys. J. Suppl. Ser.* **237**, 32 (2018).
6. H. Abdalla *et al.*, Sensitivity of the Cherenkov Telescope Array for probing cosmology and fundamental physics with gamma-ray propagation. *J. Cosmol. Astropart. Phys.* **2021**, 048 (2021).
7. F. Miniati, G. Gregori, B. Reville, S. Sarkar, Axion-driven cosmic magnetogenesis during the QCD crossover. *Phys. Rev. Lett.* **121**, 021301 (2018).
8. T. Vachaspati, Progress on cosmological magnetic fields. *Rep. Prog. Phys.* **84**, 074901 (2021).
9. D. N. Hosking, A. A. Schekochihin, Cosmic-void observations reconciled with primordial magnetogenesis. *Nat. Commun.* **14**, 7523 (2023).
10. E. S. Weibel, Spontaneously growing transverse waves in a plasma due to an anisotropic velocity distribution. *Phys. Rev. Lett.* **2**, 83 (1959).
11. B. D. Fried, Mechanism for instability of transverse plasma waves. *Phys. Fluids* **2**, 337 (1959).
12. Y. B. Fainberg, V. Shapiro, V. Shevchenko, Nonlinear theory of interaction between a monochromatic beam of relativistic electrons and a plasma. *Sov. Phys. JETP* **30**, 528 (1970).
13. L. I. Rudakov, Collective slowing down of an intense beam of relativistic electrons in a dense plasma target. *Sov. J. Exp. Theor. Phys.* **32**, 1134 (1971).
14. A. E. Broderick, P. Chang, C. Pfrommer, The cosmological impact of luminous TeV blazars. I. Implications of plasma instabilities for the intergalactic magnetic field and extragalactic gamma-ray background. *Astrophys. J.* **752**, 22 (2012).
15. R. Schlickeiser, D. Ibscher, M. Supsar, Plasma effects on fast pair beams in cosmic voids. *Astrophys. J.* **758**, 102 (2012).
16. R. Shaisultanov, Y. Lyubarsky, D. Eichler, Stream instabilities in relativistically hot plasma. *Astrophys. J.* **744**, 182 (2011).
17. A. Bret, L. Gremillet, M. E. Dieckmann, Multidimensional electron beam-plasma instabilities in the relativistic regime. *Phys. Plasmas* **17**, 120501 (2010).
18. L. O. Silva *et al.*, Interpenetrating plasma shells: Near-equipartition magnetic field generation and non-thermal particle acceleration. *Astrophys. J. Lett.* **596**, L121 (2003).
19. B. Breizman, D. Ryutov, Quasilinear relaxation of an ultrarelativistic electron beam in a plasma. *Sov. Phys. JETP* **33**, 220 (1971).
20. A. Bret, L. Gremillet, D. Benisti, Exact relativistic kinetic theory of the full unstable spectrum of an electron-beam–plasma system with maxwell-jüttner distribution functions. *Phys. Rev. E Stat. Nonlin. Soft Matter Phys.* **81**, 036402 (2010).

21. M. Axelsson *et al*., GRB221009A: The BOAT burst that shines in gamma rays. *Astrophys. J. Suppl. Ser.* **277**, 24 (2025).
22. LHAASO collaboration, Very high-energy gamma-ray emission beyond 10 TeV from GRB 221009A. *Sci. Adv.* **9**, eadj2778 (2023).
23. F. Miniati, A. Elyiv, Relaxation of blazar-induced pair beams in cosmic voids. *Astrophys. J.* **770**, 54 (2013).
24. L. Sironi, D. Giannios, Relativistic pair beams from TeV blazars: A source of reprocessed GeV emission rather than intergalactic heating. *Astrophys J* **787**, 49 (2014).
25. R. Perry, Y. Lyubarsky, The role of resonant plasma instabilities in the evolution of blazar-induced pair beams. *Mon. Not. R. Astron. Soc.* **503**, 2215–2228 (2021).
26. H. Chen, F. Fiuza, Perspectives on relativistic electron-positron pair plasma experiments of astrophysical relevance using high-power lasers. *Phys. Plasmas* **30**, 020601 (2023).
27. C. D. Arrowsmith *et al.*, Laboratory realization of relativistic pair-plasma beams. *Nat. Commun*. **15**, 5029 (2024).
28. I. Efthymiopoulos *et al*., "HiRadMat: A new irradiation facility for material testing at CERN" in *2nd International Particle Accelerator Conference, San Sebastian, Spain, 4 – 9 Sep 2011*, C. Petit-Jean-Genaz, Ed. (Proceedings of the International Particle Accelerator Conference, San Sebastian, Spain, 2011), pp. 1665–1667.
29. C. D. Arrowsmith *et al*., Generating ultradense pair beams using 400 GeV/c protons. *Phys. Rev. Res.* **3**, 023103 (2021).
30. C. Ahdida *et al*., New capabilities of the FLUKA multi-purpose code. *Front. Phys.* **9**, 788253 (2022).
31. G. Battistoni *et al*., Overview of the FLUKA code. *Ann. Nucl. Energy* **82**, 10–18 (2015).
32. V. Vlachoudis *et al*., "FLAIR: A powerful but user friendly graphical interface for FLUKA" in *Proceedings of International Conference on Mathematics, Computational Methods & Reactor Physics (M&C 2009), Saratoga Springs, New York* (American Nuclear Society, 2009).
33. C. D. Arrowsmith, A. Dyson, J. T. Gudmundsson, R. Bingham, G. Gregori, Inductively-coupled plasma discharge for use in high-energy-density science experiments. *J. Instrum.* **18**, P04008 (2023).
34. D. Ryutov *et al*., Similarity criteria for the laboratory simulation of supernova hydrodynamics. *Astrophys. J.* **518**, 821 (1999).
35. R. A. Fonseca *et al*., "OSIRIS: A three-dimensional, fully relativistic particle in cell code for modeling plasma based accelerators" in *Computational Science - ICCS 2002, International Conference Amsterdam, The Netherlands, April 21–24, 2002 Proceedings, Part III, Lecture Notes in Computer Science*, P. M. A. Sloot, A. G. Hoekstra, C. J. K. Tan, J. J. Dongarra, Eds. (Springer-Verlag, Berlin, Germany, 2002), vol. 2331, pp. 342–351.
36. A. Elyiv, A. Neronov, D. Semikoz, Gamma-ray induced cascades and magnetic fields in the intergalactic medium. *Phys. Rev. D* **80**, 023010 (2009).
37. F. A. Aharonian, TeV blazars and cosmic infrared background radiation in 27th International Cosmic Ray Conference (ICRC27). *Int. Cosmic Ray Conf.* **27**, 250 (2001).
38. A. A. Meiksin, The physics of the intergalactic medium. *Rev. Modern Phys.* **81**, 1405 (2009).
39. Z. Li *et al*., Cosmology-independent estimate of the fraction of baryon mass in the IGM from fast radio burst observations. *Astrophys. J.* **876**, 146 (2019).
40. T. Lemos, R. S. Gonçalves, J. C. Carvalho, J. S. Alcaniz, Cosmological model-independent constraints on the baryon fraction in the IGM from fast radio bursts and supernovae data. *Eur. Phys. J. C* **83**, 138 (2023).
41. L. Connor *et al*., A gas-rich cosmic web revealed by the partitioning of the missing baryons. *Nat. Astron.* **9**, 1226 (2025).
42. N. Aghanim *et al*., Planck 2018 results-VI. *Cosmol. Parameters Astron. Astrophys.* **641**, A6 (2020).
43. R. C. Davidson, D. A. Hammer, I. Haber, C. E. Wagner, Nonlinear development of electromagnetic instabilities in anisotropic plasmas. *Phys. Fluids* **15**, 317–333 (1972).
44. M. Iwamoto, E. Sobacchi, L. Sironi, Kinetic simulations of the filamentation instability in pair plasmas. *Mon. Not. R. Astron. Soc.* **522**, 2133–2144 (2023).
45. G. R. Lynch, O. I. Dahl, Approximations to multiple Coulomb scattering. *Nucl. Instr. Methods Phys. Res. Sec. B Beam Interactions Mater. Atoms.* **58**, 6–10 (1991).